Biomaterials Science

ROYAL SOCIETY OF CHEMISTRY

PAPER

View Article Online
View Journal | View Issue

Cite this: *Biomater. Sci.*, 2024, **12**, 3374

Design, clinical applications and post-surgical assessment of bioresorbable 3D-printed craniofacial composite implants†

Sara Targońska,‡[a,b] Monika Dobrzyńska-Mizera,‡[c] Maria Laura Di Lorenzo, *[d] Monika Knitter,[c] Alessandra Longo,[d,e] Maciej Dobrzyński, [f] Monika Rutkowska,[g] Szczepan Barnaś,[g] Bogdan Czapiga,[g] Maciej Stagraczyński,[g] Michał Mikulski,[h] Małgorzata Muzalewska,‡[i] Marek Wyleżoł,‡[i] Justyna Rewak-Soroczyńska,[a] Nicole Nowak,[a] Jacek Andrzejewski,[c] John Reeks[a] and Rafal J. Wiglusz *[j,a]

This study details the design, fabrication, clinical trials' evaluation, and analysis after the clinical application of 3D-printed bone reconstruction implants made of nHAp@PLDLLA [nanohydroxyapatite@poly(L-lactide-*co*-D,L-lactide)] biomaterial. The 3D-printed formulations have been tested as bone reconstruction *Cranioimplants* in 3 different medical cases, including frontal lobe, mandibular bone, and cleft palate reconstructions. Replacing one of the implants after 6 months provided a unique opportunity to evaluate the post-surgical implant obtained from a human patient. This allowed us to quantify physicochemical changes and develop a spatial map of osseointegration and material degradation kinetics as a function of specific locations. To the best of our knowledge, hydrolytic degradation and variability in the physico-chemical and mechanical properties of the biomimetic, 3D-printed implants have not been quantified in the literature after permanent placement in the human body. Such analysis has revealed the constantly changing properties of the implant, which should be considered to optimize the design of patient-specific bone substitutes. Moreover, it has been proven that the obtained composition can produce bio-mimetic, bioresorbable and bone-forming alloplastic substitutes tailored to each patient, allowing for shorter surgery times and faster patient recovery than currently available methods.

Received 7th November 2023,
Accepted 11th May 2024

DOI: 10.1039/d3bm01826a

rsc.li/biomaterials-science

[a]*Institute of Low Temperature and Structure Research, PAS, Okolna 2, PL-50-422 Wroclaw, Poland. E-mail: r.wiglusz@intibs.pl, s.targosnka@intibs.pl*
[b]*Department of Molecular Sciences, Swedish University of Agricultural Sciences, Box 7015, 75007 Uppsala, Sweden*
[c]*Institute of Materials Technology, Polymer Division, Poznan University of Technology, Piotrowo 3, 61-138 Poznan, Poland. E-mail: monika.dobrzynska-mizera@put.poznan.pl*
[d]*National Research Council (CNR), Institute of Polymers, Composites and Biomaterials (IPCB), Via Campi Flegrei, 34, 80078 Pozzuoli (NA), Italy. E-mail: marialaura.dilorenzo@ipcb.cnr.it*
[e]*National Research Council (CNR), Institute of Polymers, Composites and Biomaterials (IPCB), Via Paolo Gaifami 18, 95126 Catania, CT, Italy*
[f]*Department of Pediatric Dentistry and Preclinical Dentistry, Wroclaw Medical University, Krakowska 26, 50-425 Wroclaw, Poland*
[g]*4th Military Teaching Hospital, R. Weigla, PL-50-981 Wroclaw, Poland*
[h]*NZOZ Artdent, Piekarska 11-13, 62-800 Kalisz, Poland*
[i]*Department of Fundamentals of Machinery Design, Faculty of Mechanical Engineering Silesian University of Technology, Gliwice, Poland. E-mail: malgorzata.muzalewska@polsl.pl, marek.wylezol@polsl.pl*
[j]*Department of Organic Chemistry, Bioorganic Chemistry and Biotechnology, Silesian University of Technology, Krzywoustego 4, 44-100 Gliwice, Poland. E-mail: rafal.wiglusz@polsl.pl*

†Electronic supplementary information (ESI) available. See DOI: https://doi.org/10.1039/d3bm01826a

‡These authors contributed equally to this work.

Introduction

Tissue engineering has been developing since the 1990s as an alternative to golden standard solutions for reconstructive surgeries aiming to repair or substitute parts or even entire tissues such as cartilage, blood vessels, or bones.[1–3] Of those listed, injured or diseased bones are reconstructed most often, with the number of patients reaching two million annually. Therefore, healthcare professionals are looking for various solutions that will enable them to effectively treat patients. Four types of bone substitutes exist: autografts, allografts, xenografts and alloplasts.[4,5] Autogenous bone grafts utilise living bone tissue, usually harvested from the patient's rib or hip.[6] Allografts are obtained from cadavers, whereas xenografts originate from genetically nonidentical species.[7,8] Alloplasts are made from inert metal- or polymeric-based formulations whose properties are often boosted to achieve desired features by combining with various modifiers such as bioactive glass, hydroxyapatite (HAp), tricalcium phosphate (TCP), and calcium sulphate.[9,10] Alloplasts, like autogenous bone grafts, bear a lower risk of rejection or transmitting infectious dis-

eases in comparison to allografts or xenografts.[7,8] However, autogenous bone grafts tend to be fully resorbed without transforming into integrated bone tissues. This is a serious disadvantage because additional surgeries are required over time, which imply additional pain, extend recovery time, and cause donor bone's weakening. Bioresorbable and osteoinductive alloplasts do not have such drawbacks.[11] Additionally, customised alloplasts can be modelled to perfectly match bone defects, greatly enhancing regeneration and reconstruction processes and significantly reducing surgery time.

Additive manufacturing technology, like 3D printing, allows the creation of objects through digitally controlled deposition of successive layers of material. This technique finds large use in biomedicine and can produce patient-matched bone-substitute implants.[2,12–14] Moreover, the production of tailor-made alloplasts requires complex design and fabrication, with the involvement of an interdisciplinary team of experts that comprises doctors, engineers (mechanical, material and biomedical), chemists, and technologists. In fact, they must meet a wide range of requirements: besides reproducing the geometrical shape of the bone defect, the implant must also be resistant to loads, predict the growth of skeletal elements (especially in the case of children), exhibit appropriate resorption time, *etc*. Moreover, to develop a successful alloplastic bone substitute implant, *in vitro* and *in vivo* evaluations are needed, which must then be complemented by clinical trials.[15] For the osteoinductive potential of the implants, *in vitro* evaluation only allows for the analysis of degradation rate and mechanical performance. More detailed information can be gained *in vivo*, and an assessment can provide data on new bone formation, bone interface strength, and possible inflammatory reactions.[16]

In vivo, analysis of 3D-printed bone substitutes is generally conducted on animals like rats or rabbits. Unfortunately, this procedure does not allow for full simulation of the behaviour of the implant within the human body because several biological parameters, like water content and blood flow rate of rats and rabbits, significantly vary compared to humans.[16] Hence, clinical applications on humans are largely preferred to fully establish the medical fitness of the implants. To date, bone biopsy and computed tomography complement clinical outcomes in human patients. These techniques allow us to gain information on the dimensions and histomorphometric results of the material after months of implantation[17] but data are limited to only a small part of the implant. To the best of our knowledge, experimental data of direct analysis of the whole 3D-printed bone substitutes removed after implantation from the human body are not available in the literature, being such research available only for implants removed from animals or dealing with different materials, like 3D printed titanium and PEEK[9] or bioceramic calcium phosphate.[10]

Bioresorbable implants can be fabricated with synthetic polymers, like polylactides,[18] which are already used for clinical applications.[19] Osseointegration properties may be further enhanced by the incorporation of bioactive fillers, like nanosized hydroxyapatite (nHAp), which has biomimetic chemistry, suitable morphology, and non-immunoreactivity.[20,21] Moreover, it is bioactive, promotes cell adhesion, proliferation and increases cell viability.[20] Recently, nHAp was proven to be suitable for regenerating critical-size bone defects as it enhanced vascularisation, which is crucial in the process of new bone formation. The *in vitro* studies aimed to determine the optimal concentration of nHAp in polylactide composites based on the analysis of human adipose-derived stromal cells (hASCs) morphology, adhesion rate, and metabolic and proliferative potential. The results indicated that 10 wt% nHAp in polymeric matrix optimally improved adhesion and proliferation of hASCs, still maintaining sufficient tensile properties.[3] Further preparation and properties of a poly(L-lactide-*co*-D,L-lactide) (PLDLLA) composite containing nHAp were detailed in our previous publication as a preliminary investigation proving the usability of this material for internal bone fixation.[18]

This manuscript details the *in vitro* and clinical trials' analysis of the PLDLLA/nHAp composite used for 3D printing of personalised craniofacial implants for patients with bone defects or injuries. The novelty of this study is related to a detailed and thorough description of medical cases not reported in the literature before and a characterisation of the biomimetic and fully bioresorbable implant after use removed from the patient after 6 months of implantation. The post-surgical analysis of the implant allowed us to go beyond a mere assessment of the osteoconductive properties of the PLDLLA/nHAp composite and led to drawing a map of material degradation and overgrowth with living tissue, in dependence on the specific location of the part within the human body. The study goes towards a deeper understanding of biomaterial self-assembly, tissue healing and substitute integration within natural bone. The goal is to develop the required design criteria that meet patients' needs, which may further support the prediction and optimisation of the outcomes of such complex devices. In this case, so-called biomineralisation is apatite formation or remodelling in normal hard tissue such as bone, in diseased or atherosclerotic vessel walls, and at blood-contacting surfaces of implanted materials.

Results

The study combines *in vitro* biological analysis, designing of 3D-printed *Cranioimplants*, medical cases, and physicochemical characterisation of the implant after 6 months of permeance in the human body. The comprehensive characterisation of the nHAp@PLDLLA biomaterial was presented in our previous work.[18] The composite has a porous structure needed for bone regeneration, as pores influence cell penetration and cell distribution and, most importantly, enable the transportation of gases and nutrients into deeper layers of scaffolds.[22] The non-sterilized and non-grafted material was used as a reference (Ref), while the post-surgical parts of the implant, named nHAp@PLDLLA-Post, were utilised to trace the biosorption phenomenon.

In vitro biological tests of the nHAp@PLDLLA

Cytotoxicity of the biomimetic nHAp@PLDLLA composite was assessed through haemolysis and viability tests. Results are presented in Fig. 1, which reports the morphology of red blood cells, taken as control (Fig. 1a, b and c) and incubated with nHAp@PLDLLA (Fig. 1d, e and f) after 1, 3 and 7 days. The L929 cell line morphology and visualization of alive (blue)/dead (green) cells after 1 day (Fig. 1g), 3 days of incubation with nHAp@PLDLLA (Fig. 1h), as well as haemolysis in the presence of nHAp@PLDLLA (Fig. 1i), compared with the haemolysis caused by the solution of 1% SDS, were presented.

Despite a slight leakage of haemoglobin after 3 and 7 days (data not shown), none of the tested biomimetic compounds caused haemolysis above the approvable level (5%) (Fig. 1i).[23] The microphotographs illustrating erythrocyte morphology after incubation (1, 3, 7 days) showed no significant changes in morphology (Fig. 1a–f). Time-dependent changes are com-

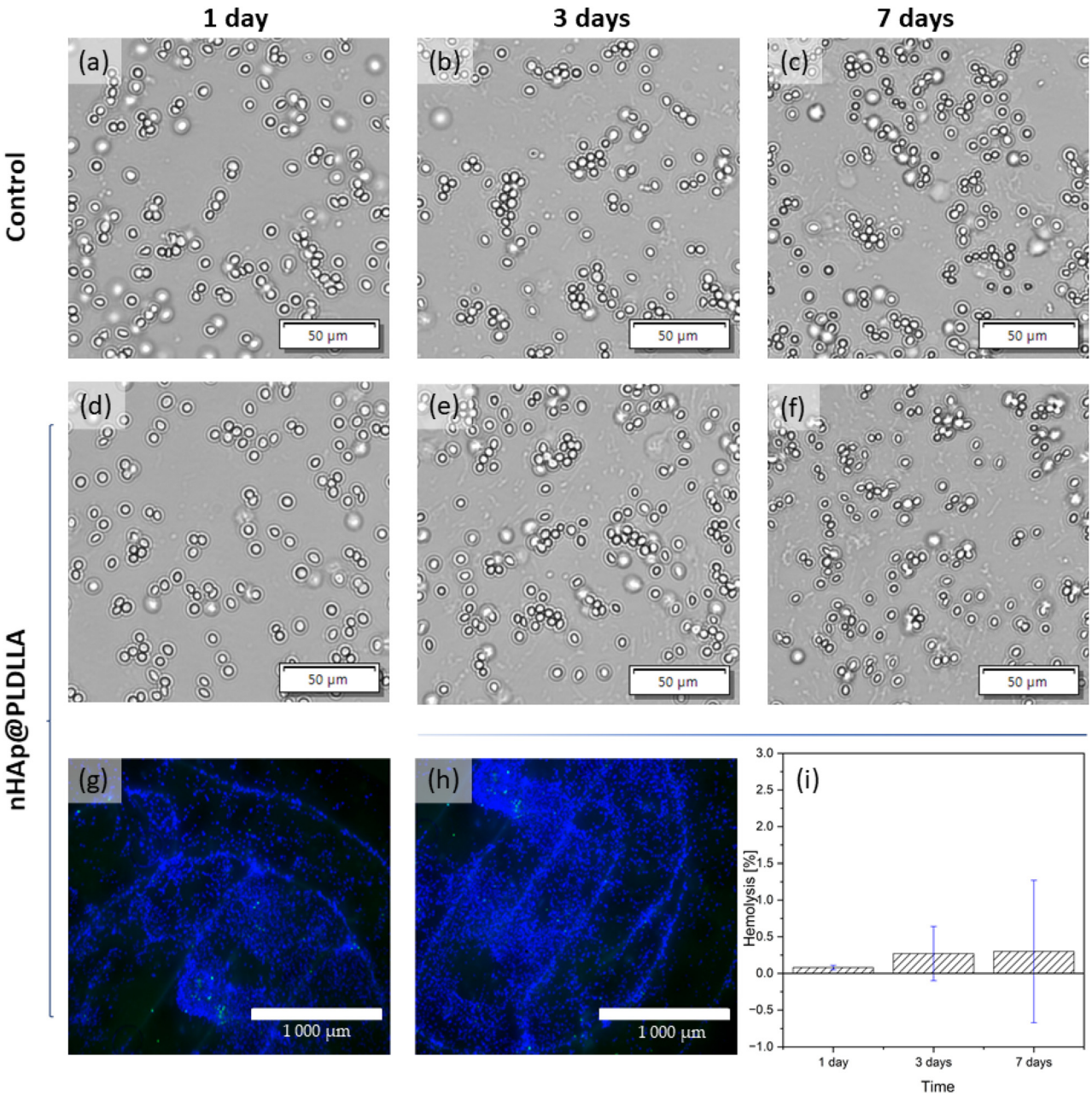

Fig. 1 Morphology of red blood cells – control (a, b and c) and incubated with nHAp@PLDLLA (d, e and f); L929 cell line morphology and visualization of life (blue)/dead (green) cells after 1 day (g) and 3 days (h) of incubation with polylactide implant scaffold nHAp@PLDLLA; hemolysis in the presence of nHAp@PLDLLA compared with the hemolysis caused by the solution of 1% SDS (i) all results were statistically significant ($p < 0.05$).

parable to those observed in the control sample. Therefore, the tested materials can be considered safe.[24]

Results indicate that the analysed polylactide scaffolds with 10 wt% of hydroxyapatite (Fig. 1g and h) are biocompatible. It can be observed that after 1 day, cells were nicely attached to the scaffold surface and created dense monolayer spots. During 3-day incubation, cell growth areas expanded further than during shorter incubation (Fig. 1h). Longer incubation yields a monolayer with wider and denser cell spots (Fig. 1h). These outcomes are highly consistent with literature studies, indicating the biocompatible properties of hydroxyapatite scaffolds,[25–29] as well as the results of biocompatibility tests carried out on animal models according to ISO 10993 - 3, 6, 10, 11 (data not shown).

Clinical trials with *Cranioimplants*

Three patients were selected for the surgeries to treat bone defects with bioresorbable and osteoconductive alloplastic implants. The 3D-printed nHAp@PLDLLA *Cranioimplants* were used to reconstruct the frontal lobe (Medical case no. 1), the mandibular bone (Medical case no. 2), and the cleft palate (Medical case no. 3) with the main aim to restore anatomical bone curvatures as well as fit the defective bone edges. The main information on the design of the *Cranioimplants* is reported and discussed in the ESI,† with the medical course presented below. All experiments were performed in accordance with the Guidelines of Declaration of Helsinki. Ethical Principles for Medical Research Involving Human Subjects were approved by the First Local Ethics Committee of Wroclaw Medical University, the Bioethics Committees at the Lower Silesian Medical Chamber, and the Greater Poland Medical Chamber, decisions no. 2/KN/2020, 3/KN/2021, 93/2022. Informed consents were obtained from human participants of this study.

Medical case no. 1: frontal lobe bone reconstruction. The bioresorbable *Cranioimplant*, precisely shaped to fulfil the bone defect, was implanted on 03/09/2020 to replace bone cement (Refobacin® Bone Cement R, Zimmer Biomet) and initiate the bone reconstruction process (Fig. 2a–c). During the two-month-long convalescence, persistent complications regarding cerebrospinal fluid leakage were observed. The leakage caused an increase in hydrostatic pressure, which further led to implant displacement and slight deformation, as revealed by CT images (Fig. 2b). It was postulated that the holed tabs designed on the implant edges (Fig. 2b,v.1) and two titanium screws ∅ = 2.0 mm (Medartis AG, Basel, Switzerland) were insufficient. Therefore, the second *Cranioimplant* was designed. On 17/02/2021, the first implant (Fig. 2b,v.1) was extracted using a raspatory under general anaesthesia. A V-shaped incision with complete excision of the previous scar was made using a blade and coagulator. The implant and fixation screws were removed. Spongostan (Ferrosan) and BioGlue® Surgical Adhesive (BioGlue) were placed under the bone edges. The bone defect was then filled with TachoSil (Corza Medical GmbH) and covered with BioGlue adhesive. The bone defect was closed with the second custom-modelled implant (Fig. 2b,v.2) and fixed with three plates (MODUS 2.0, Medartis AG, Basel, Switzerland) and twelve titanium screws ∅ = 2.0 mm (Medartis AG, Basel, Switzerland). Additionally, a drain was placed, along with a compression dressing with a Codofix (Matopat, TZMO Group, Torun, Poland). The post-operative course proceeded without complications, demonstrating the efficacy of the composite implant. Follow-up treatment was abandoned after four months as the patient decided to continue his treatment in a different reference hospital. Additional details concerning implants' modelling methodology are reported in the ESI (section S1.1).†

Most importantly, in the context of the present study, the removal of the first 3D-printed Cranioimplant made of nHAp@PLDLLA biomimetic composite allowed its thorough analysis after 6 months of permeance within the human body, as detailed below.

Medical case no. 2: mandibular bone reconstruction. An individual 3D-printed *Cranioimplant* was designed to reproduce the alveolar part of the mandible and implanted on 17/02/2021 under general anaesthesia (Fig. 2d–f). Dissection revealed two plates Reco 2.5 (KLS Martin Group) and screws ∅ = 2.0 (KLS Martin Group) connecting the mandibular body as well as significant loss of the mandibular body (approx. 31–43). Once the scar tissue was excised, the anastomoses of the mandibular body were removed. After scarification and bleeding of the bones with a drill, the defect of the mandibular bone shaft and the dentin section was reconstructed using a prepared, personalized, 3D-printed mandibular *Cranioimplant*. The implant was fixed with 4 titanium screws ∅ = 2.0 (KLS Martin Group) (Fig. 2f). The anatomical shape of the mandible bone was obtained, and stabilization was achieved. The wound was sutured in layers with 3.0 sutures, providing haemostasis. Initial post-operative course proceeded without complications, with no observed inflammatory response in the surrounding tissues, but on day 45 the patient presented a partially exposed implant. As depicted in Fig. 2e, two variants of the implant were prepared: v.1 was adapted to lower titanium plate existence, while v.2 was adjusted to the removal of both titanium plates. During the surgery, the v.1 variant was fixed, and both titanium plates were removed, which led to excessive mechanical loads being transferred to the *Cranioimplant* and its further fracture. The implant failure resulted in soft tissue perforation and its further exposure; therefore, the loose pieces were removed. It was decided to leave the intact portion of the bone implant in place. Nevertheless, the continued course of therapy and the control CBCT examination one year after the surgery exhibited newly formed bone tissue features, thus enabling the grafting of dental implants (Fig. 2f). During the dental implantation procedure, the anterior mandible section exposed newly formed native bone, differing in colour but structurally and macroscopically resembling osseous tissue. On 09/04/22, two dental implants were grafted in teeth 43 and 32, in a position that enabled their adherence to the newly formed bone in the region of vestibular bone. On 20/10/2022, the treatment was successfully completed with the prosthetic restoration of the

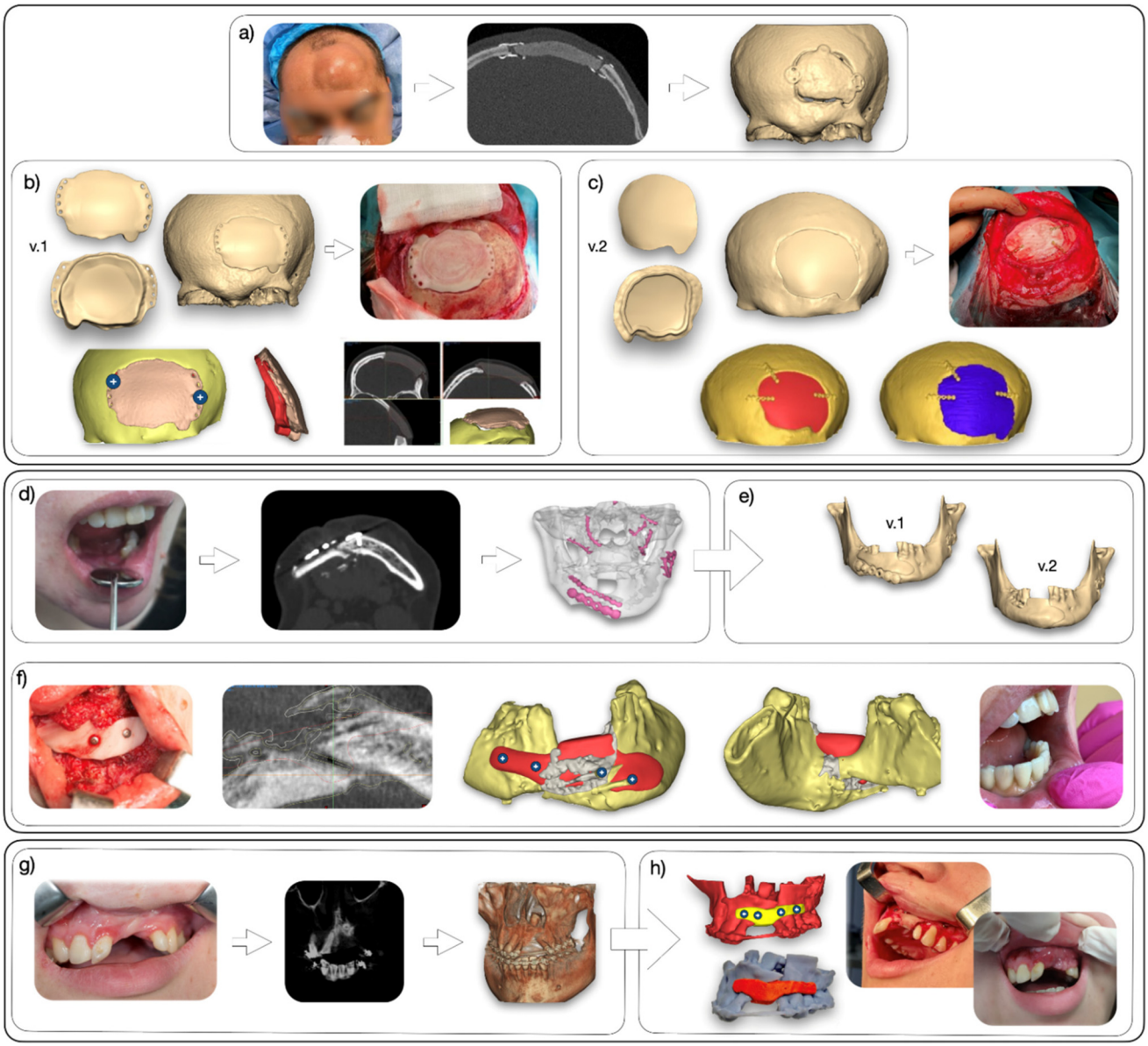

Fig. 2 Medical case no. 1 (a) view of the skull loss filled with a medical cement and commercially available Craniofix system, (b) the first version of implant model, implant model located in the bone defect and the 3D-printed implant placed in the frontal lobe, fixation of the implant, implant displacement after 6 months, (c) the second version of implant model; the implant model located in the bone defect and the 3D-printed implant placed in the frontal lobe during surgery, the implant model with its fixation (red color), the model obtained from CT scan taken 4 months after the surgery (blue color). Medical case no. 2 (d) CT scan of the patient's mandible and a 3D model of the mandible before the procedure, (e) two versions of implant models, (f) view of the patient during the operation, formation of new bone (CBCT), jaw and implant model together with newly formed bone (grey colour), view of the patient after grafting of the dental crowns. Medical case no. 3 (g) view of the patient's condition before the surgery, CT scan and jaw 3D model, (h) view of the implant model and its 3D-printed prototype in the surgical place, fixation of the implant, view of the patient during surgery and at follow-up visits.

incisors, premolars and gums on a nickel-free foundation prepared in the MPLab under the supervision of Engr. Małgorzata Malinowska and DTe Paulina Tanaś (Fig. 2f).

Therefore, the efficacy of the 3D-printed *Cranioimplant* made of nHAp@PLDLLA was proven for the specific case of mandibular bone reconstruction. Further details of the *case 2* modelling procedure are presented in ESI (section S1.2).†

Medical case no. 3: cleft palate treatment. The use of a personalized nHAp@PLDLLA implant that anatomically reproduces the region of the maxilla bone defect was proposed as an optimal clinical solution for the young patient. The surgical treatment plan assumed the reconstruction of a fragment of the alveolar process in the anterior region of the jaw. Another possibility of extensive bone augmentation by autogenous

methods was excluded; therefore, the personalized nHAp@PLDLLA *Cranioimplant* was recommended.

A personalized bone implant was implemented and fixed with 4 titanium screws ∅ = 1.5 (ChM Ltd), restoring the anatomical continuity of the maxillary alveolar (Fig. 2g). The wound was sutured in layers with 3.0 sutures, providing haemostasis. The treatment was performed in an amoxicillin cover. The postoperative course was uneventful, and the sutures were removed on day 14. During the 2-month follow-up, no inflammatory responses were noticed in the operated area (Fig. 2h).

Additional implant modelling and design details are presented in ESI (section S1.3).†

Physicochemical and structural analysis of the post-surgical *Cranioimplant*

The *Cranioimplants* were fabricated with a bioresorbable composition.[18] Therefore, they were expected to decompose within the human body with large variations in material structure and properties. Removal of the frontal lobe implant after 6 months (Medical case 1) provided the unique oopportunity to estimate changes of the 3D-printed structure and evaluate in a clinical trial, the effective performance of the implant. A wide array of experiments was conducted to quantify the evolution of the physicochemical and structural properties of the PLDLLA-based implant with respect to the original material.

Sample degradation was monitored by measuring the molar mass of pure PLDLLA copolymer, of non-sterilized 3D-printed nHAp@PLDLLA (named Ref), and of four post-surgical implant parts, named Post-1, Post-2, Post-5, Post-11, following sample position nomenclature as illustrated in Fig. 3.

The number-average molar mass (M_n), weight-average molar mass (M_w), and polydispersity ($D = M_w/M_n$) of selected samples are shown in Fig. 4a. Major reduction of molar mass was observed upon composite melt mixing and 3D printing. Both processes involve high temperatures (215 °C) and large shear, which are known for sizable degradation in polylactides[30,31] and result in a drop of M_n. The latter decreases from M_n = 332 800 Da of the as-received polymer to M_n = 74 200 Da of the 3D-printed material. Further decrease of molar mass was noticed for the post-surgical samples, with M_n dropping to about 20 000 for all samples, with no clear influence of the post-surgical site and the degradation degree. Polydispersity remains nearly constant and seems not affected

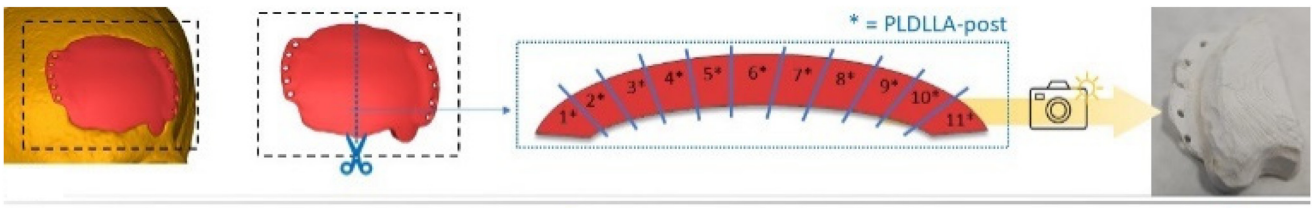

Fig. 3 Schematic illustration of post-surgical implant preparation for the physicochemical characterization.

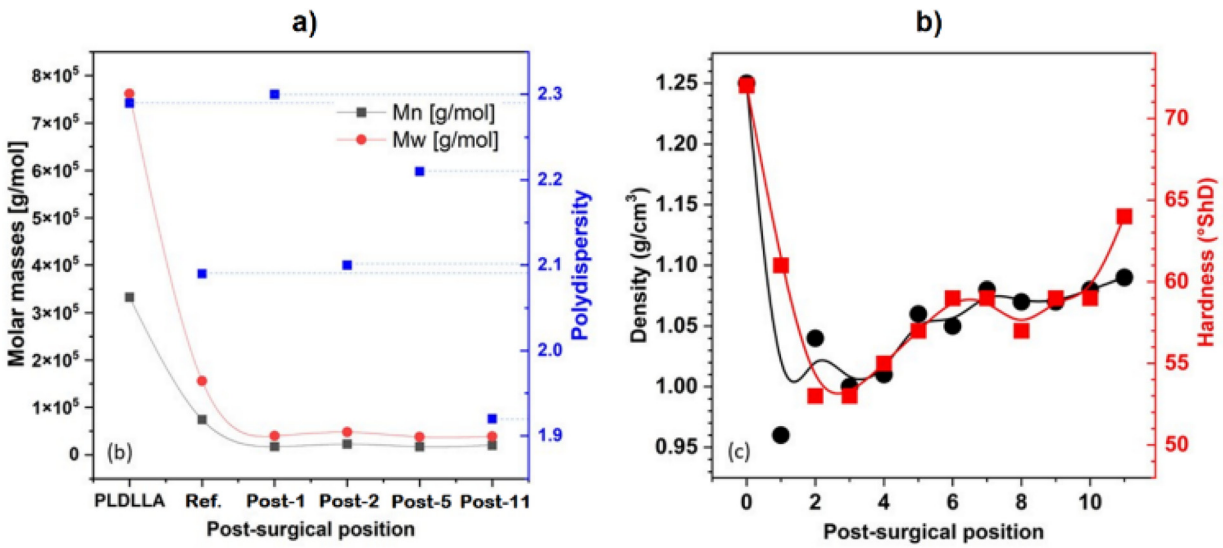

Fig. 4 (a) Number-average molar mass (M_n), weight-average molar mass (M_w) and polydispersity (D) of the as-received PLDLLA, the processed polymer (after melt mixing and 3D printing – Ref) and of the grafted material, with representative samples taken at the indicated sites (post-surgical samples); (b) density (black circles) and hardness (red squares) values for the reference nHAp@PLDLLA and post-surgical samples, reported as function of position within the implant.

by processing or 6-month grafting. This indicates that molar mass reduction is due to random chain scission.[30]

Fig. 4b shows density and hardness values for the non-sterilized reference nHAp@PLDLLA and nHAp@PLDLLA-Post samples as a function of sample position in the implant. All the post-surgical samples have lower density and hardness than the reference material. Density drops from 1.25 g cm^{-3} of the virgin material to less than 1 g cm^{-3} of the used *Cranioimplant* due to material degradation. Sample location affects degradation/remodelling as density increases from 0.96 g cm^{-3} in Post-1 (lowest value) to 1.09 g cm^{-3} in Post-11, with more remarkable changes as the distance from the skull shortens.

Significant variations in material hardness are seen in Fig. 4b. The hardness of the 3D-printed reference was around 72° ShD, with a massive drop to 53–64° ShD of post-surgical samples, depending on the location. Noteworthy, the trend of density and hardness with sample position practically overlap. The lowest hardness emerged in the top area of the frontal bone (Post-1 to Post-4). This suggests faster bone reconstruction in the skull area compared to the nasal bone area, as probed by the data detailed below.

Further analysis of material degradation was conducted by thermogravimetry (Fig. 5a), which allowed us to monitor the evolution of the implant after 6 months within the patient's body. The 3D-printed sample of nHAp@PLDLLA was examined as a reference, together with probes from the post-surgical implants. TGA was performed on samples heated at 10 K min^{-1} in an inert nitrogen atmosphere and normalized to the initial sample mass. In total, eleven samples were tested, however only selected curves were included for clarity of presentation. Non-grafted nHAp@PLDLLA (Ref) undergoes one-stage thermal decomposition at 344 °C, typical for polylactide-based materials.[32,33] Degradation of PLDLLA progresses due to chain-end cleavage, during which the polymer chain breaks at a random point in the backbone, resulting in a gradual molar mass decrease.[34–37] The nanofiller added to the composition is stable in the temperature range applied in the study and leads to the formation of a sizable residual mass. It is worth noting that pure PLDLLA decomposes entirely upon heating up to 800 °C.[38] Therefore, the residual mass originates from the amount of modifier. This proves its homogenous distribution within the polymeric matrix.

Fig. 5a also provides information on the mass-temperature profiles of samples selected from the post-operational implant. The onset temperature of degradation recorded for the post-operational samples decreased relative to the reference sample.

This is due to the partial decomposition of the PLDLLA matrix implanted into the human body. Hence, it becomes less thermally stable, as evidenced by the drop of molar mass detailed above.

The inset in the bottom-left side of the figure highlights the initial stages of degradation, showing evidence of the occurrence of multi-step events at low temperatures. The Post-11 sample starts to decompose at very low temperatures in comparison with other post-surgical samples. These pieces are located at the extreme ends of the implant and are, thereby, the most vulnerable to contact with human tissues. Another important aspect to note is the elevated residual mass (m_R) noted for the whole series of post-operational samples, compared to the value determined for the reference trial. Residual mass values largely depend on the location of the implant. The sample with the highest amount of residual mass (38%) was Post-1, being in contact with the patient's parietal bone. Going towards the eye sockets, the m_R value decreases to 17%, suggesting faster scaffold remodelling from the side of the skull. An increase in residual mass for all tested samples proves that the implant is overgrown with human tissues, structures that do not fully decompose under heating up to 800 °C.[39,40]

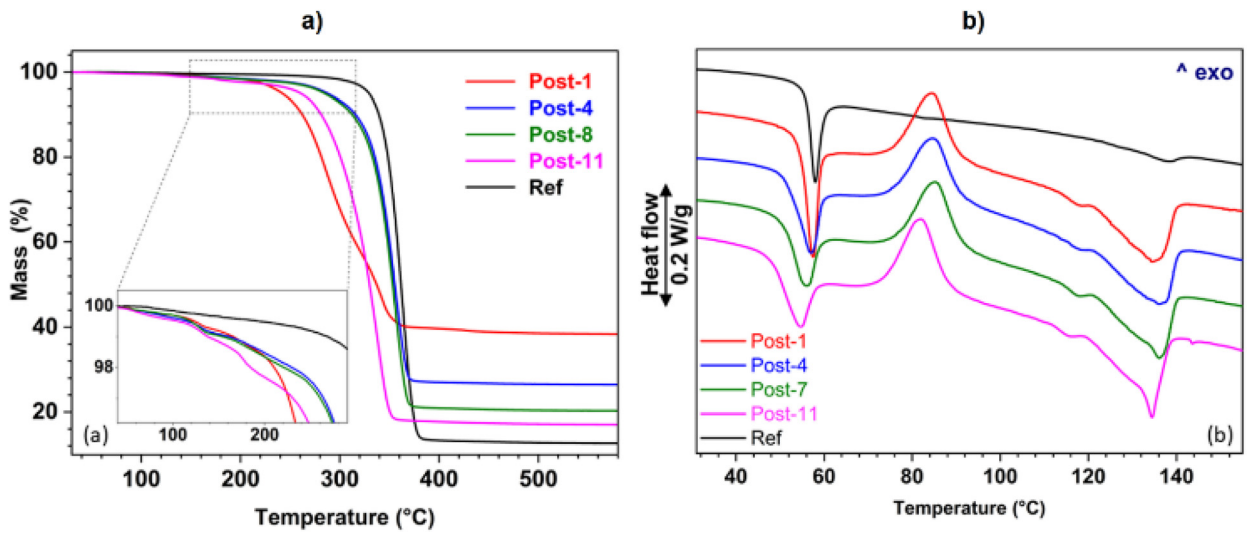

Fig. 5 (a) Thermal analysis of selected portions of the post-surgical implant, compared to non-grafted 3D-printed nHAp@PLDLLA sample (Ref): mass loss upon heating in nitrogen atmosphere; (b) heat flow rate upon heating.

Thermal analysis of the post-surgical implant was completed by calorimetry and dynamic mechanical analysis. The heat flow rate plots of the post-surgical implant upon heating at 5 K min^{-1} are presented in Fig. 5b and compared to the non-grafted 3D-printed nHAp@PLDLLA reference sample. The DSC plot of the non-grafted sample displays a glass transition (T_g) at 57.3 °C overlapped to a sharp enthalpy relaxation exotherm, peaked at 58 °C. This is typically observed in amorphous or poorly crystalline polymers when stored for prolonged times at temperatures below T_g.[41,42] Upon further heating, the DSC curve exhibits a broad and weak endotherm centred at 138.4 °C, preceded by a small shoulder at 126.7 °C. This reveals the melting of α′-crystals initially present in the sample, which, upon heating, transforms to α-modification, whose melting may overlap with possibly initially present α-crystals.[43] Comparison with enthalpy of melting of 100% crystalline PLLA[44] discloses a small crystal fraction (w_c) around 2% of the non-grafted material.

The post-surgical material shows significant variation in thermal properties, which are also influenced by the location of the grafted part (distance from nasal or parietal bone). In nHAp@PLDLLA-Post-1 (sample close to the parietal bone), the glass transition temperature and the enthalpy relaxation endotherm are slightly decreased, with T_g = 56.4 °C. After completion of the glass transition, further heating leads to cold crystallization of the polymer, revealed by an exotherm in the DSC plot that has its onset at 75.9 °C, followed by a double-peaked endotherm linked to crystal melting. Such a cold crystallisation exotherm does not appear in the non-grafted material, but is evident in all post-surgical specimens, indicating an enhanced crystallisation rate of the polymer after surgery. Comparison of the cold crystallisation exotherm and the subsequent melting endotherm reveals an initial crystallinity of w_c = 3% of the Post-1 sample, with a minor variation compared to the reference that falls within the experimental uncertainty of DSC analysis.

Increasing the distance from the parietal bone, the glass transition progressively decreases, reaching T_g = 51.4 °C in the material close to the nasal bone (nHAp@PLDLLA-Post-11). Furthermore, there is a continuous broadening of the whole glass transition range. Similarly, the onset temperature of cold crystallisation exotherm decreases with increasing distance from the parietal bone, indicating easier and faster crystallisation in these samples. However, the initial crystallinity of the material remains about 3–4% for all the analysed post-surgical specimens.

Both the decrease of T_g and faster crystallisation rate are consistent with the decreased molar mass probed by GPC, as reported in the literature for PLLA.[45,46] The PLDLLA-based plate grafted into the human body undergoes a sequence of processes. Initially, the polymer matrix starts to degrade in a gradual molar mass decrease. Next, human tissue starts to overgrow the polymeric scaffold, introducing possible nucleation sites for further crystallization. Both processes lead to enhanced crystallization kinetics. This is evident for all the post-surgical samples, indicating that six months in the human body are sufficient for partial PLDLLA decomposition and overbuilding with human tissue. This is also supported by TGA results of Fig. 5a.

Information on crystal structure and crystallinity was also gained by X-ray diffraction analysis. Fig. 6a shows the XRD patterns of the selected post-surgical fragments, reference sample, and theoretical pattern of hydroxyapatite structure. Major reflections in all spectra are to be ascribed to hydroxyapatite, as shown by comparison with the standard XRD pattern (hexagonal structure of hydroxyapatite crystals), con-

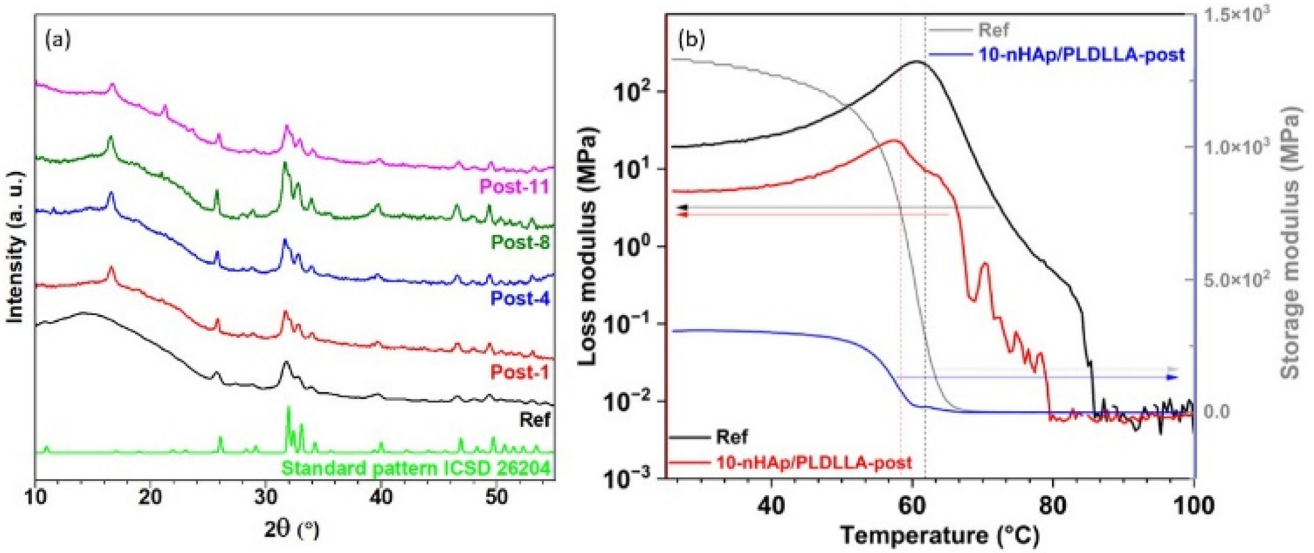

Fig. 6 (a) The X-ray powder diffraction patterns of the selected post-surgical fragments, reference sample, and theoretical pattern of hydroxyapatite structure; (b) storage and loss moduli reported for the nHAp@PLDLLA and nHAp@PLDLLA-Post samples.

firming its presence within the material in the removed implant. XRD reflections of the filler are located at 25.9° (002); 28.1° (012); 28.9° (210); 31.8° (211); 32.2° (112); 32.7° (300); 34.0° (202); 39.9° (310); 46.7° (222); 49.5° (210); 53.2° (004), with Miller index listed in the brackets.[47]

Diffraction peaks assigned to the polymer matrix are located at 16.7° (110)/(200), 18.9° (203), and 21.2° (015), and may be ascribed to either α- or α′-crystals of PLDLLA.[33] However, they are very weak. Thus, precise assignment to a specific crystal structure may appear speculative. This is because diffraction patterns of α- and α′-crystals of PLDLLA are very similar, with only minor differences in peak position. For instance, the (203) peak appears at $2\theta = 18.9°$ in α′-crystals and at $2\theta = 19.1°$ in α-form.[48] More importantly, differences in XRD spectra appear upon comparison of the implant parts with the 3D-printed reference. For the latter, the peaks expected for the PLDLLA copolymer are very weak, indicating only minor crystallinity of the sample, in agreement with the DSC data of Fig. 5b. The XRD patterns of the grafted parts display better-resolved reflections, although of weak intensity, which points to a slightly increased crystal fraction developed upon 6 months of implantation, again confirming DSC data. The slightly higher crystallinity is caused by material degradation. Since crystals are usually less susceptible to fragmentation relative to unordered areas, degradation is known to start at the amorphous chain segments.[31]

Variation in the structure of nHAp@PLDLLA upon six months of implantation in the human skull was also analysed by dynamic mechanical analysis. The PLDLLA matrix has a typical amorphous character. Therefore, its thermomechanical resistance usually does not exceed 100 °C.[18,32] Further increase in temperature causes softening of the samples and results in interruption of the experiment. However, experiments in this limited temperature range showed very significant changes in the stiffness of the implant. The storage modulus plots, presented in logarithmic scale, are shown in Fig. 6b. The elastic response of the 3D-printed reference before surgery appears much higher than that of the post-surgical implant. Apart from the obvious difference in modulus values, the curve shape also suggests changes in the glass transition temperature, as is evident in DSC results. The loss modulus peak maximum (Fig. 6b) reached about 61 °C for the reference material, while for the post-surgical sample, the peak shifted to 57 °C, which agrees with storage modulus analysis. Such changes in PLDLLA glass transition values are also observed in the DSC analysis shown in Fig. 5b. Additionally, material degradation caused large structural variations, which were confirmed by a significant drop in stiffness.

To the best of our knowledge, the results detailing the remodelling process and mechanical analysis of the bioresorbable PLDLLA-based scaffold after 6 months of remaining in the human body have not been presented in the literature to date. However, the literature presents quite a vast array of experiments conducted on animal models, proving that the grafting in ewes with poly(L-lactide-*co*-D,L-lactide) resulted in partial osseous integration after 6 months of grafting. After 36 months, the operative levels were effectively fused with surrounding areas, and the implants were completely resorbed with no adverse tissue response throughout the entire process.[49,50]

According to the Corbion datasheet, the material used in the study should be resorbed within 18 to 24 months, depending on the processing method, geometry, and grafting site. All of the above was confirmed in clinical trials. After six months of grafting, no geometry changes or collapse of the implant were noted. However, mechanical properties began to decrease, indicating the inception of resorption (Medical case no. 1). The mechanical properties of these implants were sufficient to support scaffold geometry for overgrowing tissues. The second medical case showed an implant majority rebuilt into native, bloodied bone and enabled dental grafts' placement for further toothing reconstruction. It was also confirmed that the *Cranioimplant* fragments with thickened geometry continued to degrade, which confirmed that the total resorption time exceeded 12 months. The presence of nHAp in the structure promoted osseointegration and building up of new, native bone tissue (as confirmed by post-operational TGA studies and CT scans of the patient). This effect was expected as it was previously indicated in the literature[18,51] and *in vitro* biological studies presented above. Summarizing, in our case, reconstruction of the implanted material into new bone-like tissue occurred.

Discussion

Biomimetic and bioresorbable alloplastic bone implants require complex design, production, and implantation procedures, as they must meet a wide range of requirements. They must reproduce the geometric shape of the bone defect, be resistant to loads, predict the growth of skeletal elements (especially in the case of children), exhibit appropriate resorption time, *etc*. It is a complex approach, made possible by the involvement of an interdisciplinary team including doctors, mechanical, material, and biomedical engineers, chemists, and technologists.

Successful design, production and implantation were proved for three different medical cases. The virtual versions of the implant models were used for production *via* FDM 3D printing technology, with craniofacial parts and trial implant models produced for each patient. The latter could be evaluated by the doctors and used to illustrate the surgical plan to the patients, thus greatly increasing their awareness. Physical models could also allow the doctors to assess the implants, suggest corrections to the models, and plan the exact course of the operation, *e.g.* simulated cutting or fixation places. This process allows the doctor to better prepare for often complicated operations and, in turn, reduce the operating time required to perform the surgery.

Notably, the perfect implant fit and practised medical crew enabled practitioners to significantly reduce the operational time by 50 to 70% for the medical procedures presented herein compared to autografting or allografting methods. More importantly, the cleft palate surgery was carried out in

the dentist's office. To minimize the inflammation risk, the manufacturing process was carried out in accordance with ISO standards (ISO-13485 Medical devices – Quality management systems – Requirements for regulatory purposes) and the implants were subjected to radiation sterilization.

In the case of patient no. 1 (frontal lobe bone reconstruction), scaffold degradation assisted with bone reconstruction at the site was observed, as probed by a wide array of material analyses detailed above. In the case of the second patient (mandibular bone reconstruction), the CT scan, performed one year after the *Cranioimplant* surgery, revealed that the PLDLLA-based implant was partially resorbed within the mandible, and new bone tissue had been formed. This assumption was confirmed during the dental implants' placement when new, bloodied bone tissue was noticed after the gingiva incision. The surgeon confirmed that a large part of the *Cranioimplant* had been resorbed, except for its thickest parts, which were still visible, well-fixed, and free from inflammations. The appearance of the patient's prosthetic restoration is shown in Fig. 2d. Monthly checks confirmed the absence of inflammation and a properly running healing process.

From a material point of view, the *Cranioimplant* is safe, bioresorbable, and able to remodel into natural bone, as confirmed by *in vitro* studies and clinical trials. These results were also confirmed in a wide range of biocompatibility tests carried out on animal models, not presented in the article, according to ISO 10993 (Parts – 3, 6, 10, 11). Removal of the frontal lobe implant after 6 months after implantation allowed us to estimate changes of the 3D-printed structure and evaluate remodelling upon *in vivo* grafting. The composite material underwent a partial resorption/decomposition process, strictly dependent on implant location. The rate of degradation/remodelling processes increased as the distance from the skull decreased. The degradation process is associated with structural changes taking place in the polymeric matrix. This overlaps with overgrowth in human tissues, which has been proved for postsurgical samples. As depicted in Fig. 2b, complications that occurred in the case of frontal lobe bone reconstruction led to the implant displacement, especially its bottom part (perspective from the nasal bone side). This, in turn, caused a non-uniform connection between the implant and native osseous tissue, limiting the *Cranioimplant* overgrowth (Post-8 to Post-11 samples) with human tissue in the healing course. The obtained results may vary among patients, as there are many factors influencing the remodelling process, including implant size and thickness, fixation method, implantation area, types of polymeric matrix and modifier used, up to general health condition, or the age of the patient.

Materials and methods

Materials

The implants were produced using commercially available poly (L-lactide-*co*-D,L-lactide) (Purasorb PLDL 8058, L-lactide/DL-lactide) copolymer (PLDLLA), provided by Corbion, and nano-sized hydroxyapatite (nHAp) obtained *via* wet chemical precipitation process. A composite made of 10 wt% nHAp and 90 wt% PLDLLA (nHAp@PLDLLA) was prepared as detailed in ref. 18, with its structure, morphology and mechanical properties also presented and discussed. All materials and procedures used in the study possess FDA certificate or Bioethics Committee of the Greater Poland Medical Chamber approval. The innovative bioresorbable implants for bone reconstruction were developed, and named *Cranioimplants*.

Filament production

The process of filament production began with mixing of PLDLLA with 10 wt% of nHAp in a rotary mixer Retsch GM 200 for 3 min at a rotation speed of 2000 rpm. Homogenizing of the premixed and vacuum-dried (50 °C; 24 h) materials was ensured by molten state extrusion with a co-rotating twin-screw extruder (Model EH16.2D), produced by Zamak, Poland, operated at 210 °C and 60 rpm. The extruded rod was cooled in air and pelletized. Then the filament shaping step was conducted on a single-screw extruder, type W25-30D, produced by Metalchem, Poland, equipped with a 25 mm screw and L/D = 34. During the process, the hopper was equipped with a membrane dryer (KOCH-Technic, Germany) that was set at 55 °C. The extrusion line also included a dry conveyor belt and a spool winder dedicated to the polymer filament extrusion process. These were both designed by the Institute of Polymer Materials and Dyes in Torun (Poland). The shaping head temperature was 215 °C with the following temperature profile throughout the extruder barrel: 215 °C/210 °C /200 °C/180 °C. To achieve the targeted filament diameter of 1.75 mm, the extrusion was stretched slightly as the head nozzle size was 2 mm. The rotational speed of the screw was set at 15 (±2) rpm, and the linear speed of the extrusion process was 3 (±0.5) m min^{-1}.

Biological tests of the nHAp@PLDLLA composite (*in vitro* trial)

Haemolysis assay and tests of biological properties were conducted to evaluate cytotoxicity of the nHAp@PLDLLA composite, which is a crucial characteristic for biomaterials. Haemolysis assay was performed according to the standard protocol with slight modification.[52] Erythrocyte fraction was obtained by purification of ram blood (ProAnimali, Wroclaw, Poland) through centrifugation (3000 rpm, 10 min) and washing with the saline. The process was repeated three times to remove residual preservatives and other blood fractions. The blood was mixed with fresh saline (1 : 1 v/v). The tested filament (nHAp@PLDLLA) was cut evenly into 1 cm (0.02625 g) pieces and placed in tubes where 1 ml of purified erythrocyte fraction was added. Pure erythrocyte fraction was used as a control. All experiments were performed in triplicate, and the samples were incubated at 37 °C for 1, 3, and 7 days. The contents of the tubes were gently mixed by inversion each day to maintain direct contact between the red blood cells and the material. After incubation, the samples were set aside to ensure gravity-induced separation of the phases without the

use of a centrifuge, to avoid mechanical damage to the erythrocytes caused by the filament during centrifugation. The supernatant was then transferred to a microplate, and the optical density was measured at 540 nm using a plate reader (Varioskan LUX, Thermo Fisher Scientific, USA). Statistical analysis was performed using a one-way ANOVA test ($p < 0.05$). The percentage of haemolysis was calculated from the following formula (1):

$$\text{Hemolysis} = ((\text{sample absorbance} - \text{negative control absorbance}))/(\text{positive control absorbance-negative control}) \cdot 100 \quad (1)$$

The remaining red blood cell fraction (after collecting the supernatant) was used for microscopy. 2 μl of each sample was smeared on a slide and observed under a microscope (Olympus IX83 Fluoview FV1200, Hamatsu C13440 CCD camera, 20× magnification) in order to assess the effect of the material on erythrocyte morphology.

Cell culture and viability assay

The tested biomimetic filament (nHAp@PLDLLA) with 10 wt% hydroxyapatite composition was sterilized under UV light for 30 minutes prior to the cell culture and viability assay. This standard sterilization technique is commonly used for materials which cannot be sterilized *via* other laboratory techniques such as autoclaving. Mouse fibroblast (L929, ATCC) cell lines were maintained in high glucose DMEM (4.5 g mL^{-1}) without phenol red, which was supplemented with 10% FBS (FBS, South America origin, Biowest) and 2 mM L-glutamine and 25 μg mL^{-1} gentamicin (Biowest). Cell lines were incubated in standard conditions of 5% CO_2 in a humified atmosphere of 95% air and 5% CO_2 at 37 °C. L929 cells were passaged with TrypLE (Thermo scientific, TrypLE™ Express Enzyme (1×), no phenol red) solution once per week. The cell line was subcultured three times before the experiment took place.

To evaluate cell morphology, mouse fibroblasts were seeded at a density of 5×10^4 per well in a 12-well plate and incubated with nHAp@PLDLLA. Cylindrical 3D-printed samples 5 mm in diameter and 2–3 mm in thickness (0.214–0.320 g) were used in biological assay. After incubation periods of 24 and 72 hours, cells and nHAp@PLDLLA filament were washed with sterile PBS, and then fresh PBS was added to each well. Invitrogen™ ReadyProbes™ Cell Viability Imaging Kit (Blue-live/Green-dead) was then used to visualize the dead–live cell ratio. Furthermore, cell morphology was captured by using Invitrogen™ EVOS™ FL Digital Inverted Fluorescence Microscope (×10 magnification).

Modelling of the *Cranioimplants*

The development of the implant starts with the design of an anatomical structure model, which is prepared with Materialise Mimics 23.0 software. Anatomical structures were obtained from medical imaging examinations, such as computed tomography (CT) or magnetic resonance imaging (MRI), which provided the planned cross-sections of anatomical structures that were then transformed into a three-dimensional model.[53–58] DICOM files (Digital Imaging and Communications in Medicine) were used.

Once the patient's anatomical structure was modelled, the implant was built with the voxel haptic system – Geomagic Freeform Plus 2021, interfaced with Touch X v. 2021 model arm.[59] This intuitive device allows for haptic coupling of a user with the system, aiding in modelling complex geometries such as biomimetic anatomical structures.

Cranioimplant production by 3D printing

3D printing was carried out *via* standard Fused Deposition Modelling (FDM), using a Prusa MK3 machine (from PrusaResearch, Czech Republic). The machine was equipped with a 0.4 mm brass nozzle and worked in the direct drive system. The bed table temperature was set at 60 °C, while the nozzle temperature was 215 °C. The PrusaSlicer software was used to generate the model machine code (g-code) with a single layer thickness of 0.15 mm. The two-layer external shell was designed. The models were printed with full infill (100%), while individual layers intersected at an angle of 90 °C. Additional analyses of printing accuracy are presented in the ESI file.†

The sterilization process was conducted at the Institute of Nuclear Chemistry and Technology – Radiation Sterilization Station for Medical Devices and Allografts in Warsaw, Poland. Bone implants were sterilized *via* radiation using high-energy electrons. For this purpose, the "Elektronika" accelerator producing an electron beam with an energy of 10 MeV and an average power of 10 kW was used per ISO 13485: 2016 standard. The dose of ionizing radiation used was 36 kGy. The implants were packed in labelled cardboard boxes prior to the sterilization procedure, ensuring their sterility until the transplantation procedure. A schematic diagram of the *Cranioimplant* production procedure is presented in Fig. 7.

Chemical, physical and structural characterization of the post-surgical *Cranioimplant*

Extraction of the frontal lobe biomimetic bone implant (Medical case no. 1) allowed for a detailed analysis of the physicochemical properties of the PLDLLA-based implant after a six-month implementation period in the human patient. The explanted *Cranioimplant*, with no surrounding tissue attached, was disinfected with an alcohol-based solution, placed in a sterile box and refrigerated at 4 °C. The removed implant was divided into 11 pieces and labelled from nHAp@PLDLLA-Post1 to nHAp@PLDLLA-Post11. Enumeration of the implant sections begins with the part connecting to the parietal bone (nHAp@PLDLLA-Post1) and ends with the part close to the nasal bone (nHAp/PLDLLA-Post11).

Changes in molar mass of PLDLLA polymeric matrix were evaluated *via* gel permeation chromatography (GPC) technique using a multiangle light scattering detector (λ = 690 nm) DAWN EOS (Wyatt Technologies) equipment with a refractive index detector, Dn-2010 RI from WGE Dr Bures. Before the

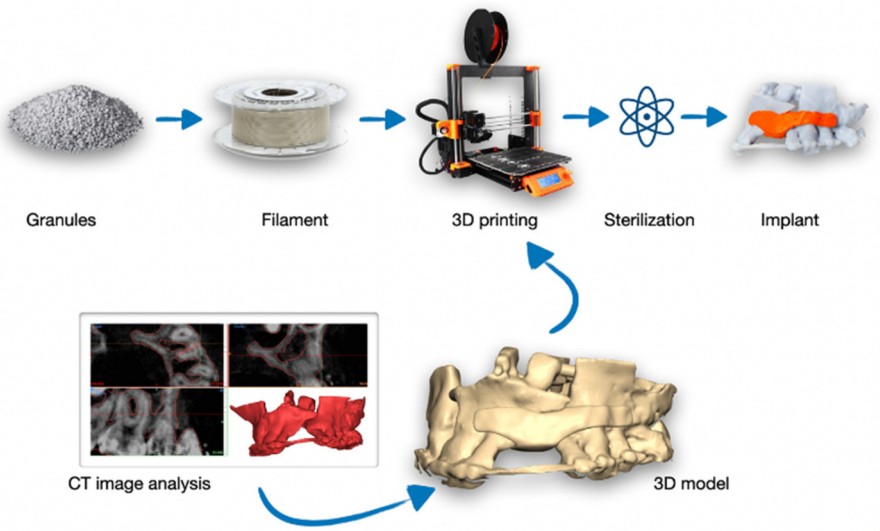

Fig. 7 General diagram of the *Cranioimplant* manufacturing process.

analysis, the samples were dissolved in THF (Tetrahydrofuran). Measurements were performed with the following set of columns: guard, PSS 100 Å, PSS 500 Å, PSS 1000 Å, and PSS 100 000 Å (Polymer Standard Service) using polystyrene standards at the temperature of 35 °C. The dispersity indexes (D) were counted according to eqn (2):

$$D = M_W/M_N \quad (2)$$

where, D is a dispersity index, M_W is the weight-average molar weight, and M_N is the average molecular weight. Measurements were collected for the nHAp@PLDLLA-Post1, nHAp@PLDLLA-Post2, nHAp@PLDLLA-Post5, and nHAp@PLDLLA-Post11.

Changes in the crystal structure of the *Cranioimplant* were evaluated *via* X-ray diffraction (XRD). The XRD patterns were collected by the X'Pert Pro PANalytical diffractometer (Cu, Kα1 = 1.54060 Å) (Malvern Panalytical Ltd, Malvern, UK) in the range of 2θ between 10° and 55° at room temperature. The measurement data were normalized between 0 and 1 value.

Thermogravimetric analysis (TGA) was employed to assess the possible degradation of the polymeric matrix and the appearance of new tissue in the implant structure, which was expected during the rebuilding process. TGA analysis of the post-surgical implant was performed according to previously used methodology.[18,32] The temperature range was set between 30 and 800 °C at a heating rate of 10 K min^{-1} in a nitrogen atmosphere using a Netzsch TG 209 F1 apparatus. The instrument was calibrated with high purity standards, including In, Sn, Bi, Zn, Al and Ag. An auto-calibrated, built-in balance was used to prepare 11 samples of 8 ± 1 mg. These samples were then placed into ceramic pans. The decomposition onset temperature T_o was determined at the intersection of two branch tangents of the thermogravimetric curve.[33] The mass gained at the end of the measurement (m_R) was evaluated to assess the amount of the residual content remaining in the sample pan reached after heating at 800 °C. Each measurement was preceded by an empty pan run. The empty run value was subtracted from each thermogram to compensate for instrumental drift.

Thermal properties of the post-surgical implant were investigated with a Q2000 T_{zero} differential scanning calorimeter (DSC) produced by TA Instruments, equipped with an RCS90 cooling accessory. The temperature and heat-flow rate signals of the calorimeter were calibrated by analysis of the extrapolated onset temperature and area of the melting point of indium, respectively. Measurements took place at a heating rate of 5 K min^{-1}. Dry nitrogen gas was used to purge the sample environment at a flow rate of 30 mL min^{-1}. Each 6 mg sample was sealed in T_{zero} hermetic pans and then heated from 0 to 180 °C at a rate of 5 Kmin^{-1}, allowing for the analysis of the glass transition, cold crystallization and melting behaviour.

Mechanical properties of the post-surgical implant were assessed by using hardness and density tests. The shore hardness test was conducted with a hardness tester Zwick according to PN-EN ISO 868: 2005.[60] The density measurements were conducted by the hydrostatic method according to the PN-EN ISO 1183-1 standard.[18,61] The measurement began with the sample being weighed in the air, followed by the weighting of the ethyl alcohol. The density was further calculated according to eqn (3):

$$\rho = \frac{m_p}{m_{ci} - m_p} \cdot \rho_{ci} \quad (3)$$

where: ρ – sample density [g cm^{-3}], m_p – sample mass in the air [g], m_{ci} – sample mass in an immersion liquid [g], ρ_{ci} – immersion liquid density [g cm^{-3}].

The measurements were carried out at 23 °C on a laboratory balance with an accuracy of 0.0001 g, equipped with a hydrostatic adapter to determine the solids' and liquids' density.

The thermomechanical analysis (DMA) was conducted to determine changes in the post-surgical *Cranioimplant* structure. The measurements were conducted according to the previously used methodology.[32] The experiment started at 298 K with a heating rate of 2 K min^{-1}, the applied strain of 0.01%, and a frequency of 1 Hz. The sample was cut out from the post-surgical implant; thus, the dimensions were reduced to 30 × 10 × 4 mm. For comparison purposes, an identical implant was made of the nHAp@PLDLLA reference material, from which the same shape was cut out.

Clinical trials

Medical case no. 1. Frontal lobe bone reconstruction. The first patient, aged 43, was hospitalized with a neoplasm in the area of the frontal sinus, which was 23 × 38 × 27 mm in size. This caused bone osteolysis in the frontal bone. The tumour was removed, and the bone loss was initially filled with bone cement.

Medical case no. 2. Mandibular bone reconstruction. A 33-year-old patient was hospitalized in the intensive care unit due to a car accident (May 2019). The patient sustained multi-organ trauma, including extensive multi-fragment fractures of the craniofacial bones in the middle and lower levels of the face. The patient was admitted to the hospital in severe general condition, and neurological assessment rated the patient 3 on the Glasgow Coma Scale. After stabilization of the patient's general condition, reconstruction and osteosynthesis of the craniofacial bone using titanium plates commenced (Fig. 2d). Clinical evaluation and radiological analysis revealed a significant defect in the mandibular bones and joint socket. Furthermore, teeth 43 to 31 were missing, and there was a shallowing of the vestibule of the oral cavity and numerous scar puffs within the floor of the oral cavity, disrupting the normal anatomy in this area. To restore the impaired functions of the oral cavity and obtain satisfactory aesthetic results, treatment should account for the extent of the trauma and bone defects in the mandible and the unfavourable conditions for bone regeneration related to the morphological state of the surrounding soft tissue. During convalescence, the patient complained of difficulties with proper physiological functioning, resulting from, among others, a post-traumatic bone defect of the mandibular body, which caused disfigurement, loss of toothing and facial aesthetics. Additionally, the patient exhibited reduced self-acceptance due to the distorted facial profile, impaired articulation function and the correct intake and chewing of food.

The analysis of the resulting 3D models defined strict requirements for the selection of treatment methods. The unfavourable topography of the bone defect, *i.e.* polyhedral defect shape as well as mobile and scarred soft tissues, caused additional difficulties. Traditional reconstructive methods using autogenous bone were considered. Since it would require another surgical site, this plan was not accepted by the patient. The most reasonable option turned out to be the use of an individual *Cranioimplant*.

Medical case no. 3. Cleft palate treatment. A 16-year-old patient needed surgical treatment of a bone defect in the maxillary alveolar process, as well as stabilization of the incisive bone. The treatment goal would be to restore the function and aesthetics of the anterior part of the maxilla *via* prosthetic reconstruction. The patient was referred by the orthodontics facility of the Medical University in Wroclaw and did not reveal any systemic diseases or allergies. Intraorally present bilateral cleft palate according to Kernahan and Stark classification – Cleft primary and secondary palate involving the lip, alveolar process and palate was recognized. The last surgery of the multi-stage cleft treatment was performed when the patient was 14 years of age. The procedure consisted of reconstruction of the maxillary alveolar process using an autologous graft using bone from the iliac plate. The grafted hip bone was completely resorbed in the post-operative period.

The clinical examination found postoperative scars on the skin in the upper lip area as well as some asymmetry. Furthermore, intraorally, there were missing anterior teeth. Microdontic teeth were also present in tooth positions 21 and 22. Other noteworthy postoperative complications were: an active palatal fistula, impaired articulation function with respect to biting and chewing food, and a visible aesthetic defect. The patient would undergo orthodontic treatment with an unfavourable prognosis to restore the full function of the stomatognathic system.

Conclusions

The study detailed in this manuscript includes the medical cases' planning and modelling of biomimetic bone-reconstruction implants, surgical procedures, and pre- and post-surgical analysis. The process allowed for the creation of very precise implant shapes tailored to the patients' defects and, in turn, for a reduction of the duration of the surgical procedures. It was proved that at the modelling stage, apart from implant shape, it is crucial to properly design the fixation route in consultation with the surgeon. Patients' follow-up visits, together with *in vitro* test results, confirmed that the *Cranioimplants* were non-toxic and biocompatible. From the application point of view, examination of the post-surgical implant indicated that the biomaterial started its degradation and was overgrown with living tissue, showing biomimetic and osteoconductive properties. It was possible to implement further treatment and prosthetic restorations at the site of the newly developed, bloodied bone.

These implantation trials bring hope for further perspectives in the field of alloplastic, patients'-tailored implants, together with subsequent scheduled surgeries. This reinforced material composed of nHAp@PLDLLA can be utilized as internal bone fixation implants in many medical fields, including orthopaedic, oral, maxillofacial, craniofacial, and plastic and reconstructive surgeries.

Author contributions

Sara Targońska: conceptualization, investigation, methodology, visualization, writing – original draft, writing – review & editing. Monika Dobrzyńska-Mizera: conceptualization, investigation, methodology, funding acquisition, writing – original draft, writing – review & editing. Monika Knitter: investigation, methodology, funding acquisition, writing – original draft. Maria Laura Di Lorenzo: investigation, writing – review & editing. Alessandra Longo: writing – review & editing. Maciej Dobrzyński: investigation. Monika Rutkowska: investigation, methodology. Szczepan Barnaś: investigation, methodology. Bogdan Czapiga: investigation, methodology. Maciej Stagraczyński: investigation, methodology. Michał Mikulski: investigation, methodology. Małgorzata Muzalewska: methodology, visualization, funding acquisition, writing – original draft. Marek Wyleżoł: methodology, visualization, funding acquisition, writing – original draft. Justyna Rewak – Soroczyńska: investigation, methodology, writing – original draft. Nicole Nowak: investigation, methodology, writing – original draft. Jacek Andrzejewski: investigation, methodology, writing – original draft. John M. Reeks: writing – review & editing. Rafal J. Wiglusz: idea and conceptualization, investigation, methodology, funding acquisition, visualization, project administration, supervision, writing – original draft, writing – review & editing.

Conflicts of interest

There are no conflicts to declare.

Acknowledgements

This work was financially supported by the National Science Centre Poland (NCN) under the Project 'Biocompatible materials with theranostics' properties for precision medical application' (No. UMO-2021/43/B/ST5/02960), the National Centre for Research and Development (NCBR) (POIR.01.01.01-00-0646/19-00), and the Poznan University of Technology (No. 0613/SBAD/4770, and 0912/SIGR/8058). The authors would like to acknowledge the Foundation for Polish Science (FNP) (No. START 083.2022) and Syntplant sp. z o.o. (Poland) for a delivery of a commercial PLDLLA (Purasorb, L-lactide/DL-lactide copolymer, ratio: 80/20). Italian National Research Council (CNR) Short-Term Mobility Program is also acknowledged.

References

1 T. G. Kim, H. Shin and D. W. Lim, *Adv. Funct. Mater.*, 2012, **22**, 2446–2468.
2 A. S. Greenwald, S. D. Boden, V. M. Goldberg, Y. Khan, C. T. Laurencin, R. N. Rosier, American Academy of Orthopaedic Surgeons. and The Committee on Biological Implants, *J. Bone Jt. Surg., Am. Vol.*, 2001, **83**, 98–103.
3 K. Marycz, A. Smieszek, S. Targonska, S. A. Walsh, K. Szustakiewicz and R. J. Wiglusz, *Mater. Sci. Eng., C*, 2020, 110634.
4 J. Russias, E. Saiz, R. K. Nalla, K. Gryn, R. O. Ritchie and A. P. Tomsia, *Mater. Sci. Eng., C: Biomimetic Supramol. Syst.*, 2006, **26**, 1289–1295.
5 S. Targonska, S. Dominiak, R. J. Wiglusz and M. Dominiak, *Nanomaterials*, 2022, **12**, 3752.
6 G. Fernandez de Grado, L. Keller, Y. Idoux-Gillet, Q. Wagner, A.-M. Musset, N. Benkirane-Jessel, F. Bornert and D. Offner, *J. Tissue Eng.*, 2018, **9**, 1–18.
7 K. Tilkeridis, P. Touzopoulos, A. Ververidis, S. Christodoulou, K. Kazakos and G. I. Drosos, *World J. Orthop.*, 2014, **5**, 30–37.
8 K. Saikia, T. Bhattacharya, S. Bhuyan, D. Talukdar, S. Saikia and P. Jitesh, *Indian J. Orthop.*, 2008, **42**, 169–172.
9 L. Kihlström Burenstam Linder, U. Birgersson, K. Lundgren, C. Illies and T. Engstrand, *World Neurosurg.*, 2019, **122**, e399–e407.
10 J. Sundblom, F. Xheka, O. Casar-Borota and M. Ryttlefors, *J. Neurosurg. Case Lessons*, 2021, **1**, 1–5.
11 M. L. Wickramasinghe, G. J. Dias and K. M. G. P. Premadasa, *J. Biomed. Mater. Res., Part B*, 2022, **110**, 1724–1749.
12 H.-I. Kim, N. Raja, J. Kim, A. Sung, Y.-J. Choi, H. Yun and H. Park, *Mater. Des.*, 2022, **219**, 110793.
13 C. Ghayor, I. Bhattacharya, J. Guerrero, M. Özcan and F. E. Weber, *Materials*, 2022, **15**, 1433.
14 K. K. Lee, N. Raja, H. Yun, S. C. Lee and C.-S. Lee, *Acta Biomater.*, 2023, **159**, 382–393.
15 D. Zhao, F. Witte, F. Lu, J. Wang, J. Li and L. Qin, *Biomaterials*, 2017, **112**, 287–302.
16 P. Sekar, N. S and V. Desai, *J. Magnesium Alloys*, 2021, **9**, 1147–1163.
17 P. Mekcha, J. Wongpairojpanich, F. Thammarakcharoen, J. Suwanprateeb and B. Buranawat, *J. Prosthodont Res.*, 2023, **67**, 311–320.
18 S. Targonska, M. Dobrzynska-Mizera, M. Wujczyk, J. Rewak-Soroczynska, M. Knitter, K. Dopierala, J. Andrzejewski and R. J. Wiglusz, *Eur. Polym. J.*, 2022, **165**, 110997.
19 J. M. Schakenraad, P. Nieuwenhuis, I. Molenaar, J. Helder, P. J. Dijkstra and J. Feijen, *J. Biomed. Mater. Res.*, 1989, **23**, 1271–1288.
20 A. Smieszek, K. Marycz, K. Szustakiewicz, B. Kryszak, S. Targonska, K. Zawisza, A. Watras and R. J. Wiglusz, *Mater. Sci. Eng., C*, 2019, **98**, 213–226.
21 K. Szustakiewicz, M. Gazińska, B. Kryszak, M. Grzymajło, J. Pigłowski, R. J. Wiglusz and M. Okamoto, *Eur. Polym. J.*, 2019, **113**, 313–320.
22 C. Wang, W. Huang, Y. Zhou, L. He, Z. He, Z. Chen, X. He, S. Tian, J. Liao, B. Lu, Y. Wei and M. Wang, *Bioact. Mater.*, 2020, **5**, 82–91.
23 N. P. Aditya, G. Chimote, K. Gunalan, R. Banerjee, S. Patankar and B. Madhusudhan, *Exp. Parasitol.*, 2012, **131**, 292–299.

24 A. Remigante, R. Morabito and A. Marino, *Antioxidants*, 2019, **9**, 25.
25 N. Ramesh, S. C. Moratti and G. J. Dias, *J. Biomed. Mater. Res., Part B*, 2018, **106**, 2046–2057.
26 H. Lin, C. Yin, A. Mo and G. Hong, *Materials*, 2021, **14**, 235.
27 Z. Bal, T. Kaito, F. Korkusuz and H. Yoshikawa, *Emergent Mater.*, 2020, **3**, 521–544.
28 B. Huang, G. Caetano, C. Vyas, J. Blaker, C. Diver and P. Bártolo, *Materials*, 2018, **11**, 129.
29 A. Bianco, B. M. Bozzo, C. Del Gaudio, I. Cacciotti, I. Armentano, M. Dottori, F. D'Angelo, S. Martino, A. Orlacchio and J. M. Kenny, *J. Bioact. Compat. Polym.*, 2011, **26**, 225–241.
30 P. E. Le Marec, L. Ferry, J. C. Quantin, J. C. Bénézet, F. Bonfils, S. Guilbert and A. Bergeret, *Polym. Degrad. Stab.*, 2014, **110**, 353–363.
31 A. Mirza, J. Bove, J. Litwa and G. Appelbe, *J. Hand. Microsurg.*, 2016, **04**, 77–80.
32 M. Dobrzyńska-Mizera, M. Knitter, S. Mallardo, M. C. Del Barone, G. Santagata and M. L. Di Lorenzo, *Materials*, 2021, **14**, 2569.
33 M. Dobrzyńska-Mizera, M. Knitter, A. Woźniak-Braszak, M. Baranowski, T. Sterzyński and M. L. Di Lorenzo, *Materials*, 2020, **13**, 3776.
34 A. Södergård and J. H. Näsman, *Ind. Eng. Chem. Res.*, 1996, **35**, 732–735.
35 M. L. Di Lorenzo and A. Longo, *Thermochim. Acta*, 2019, **677**, 180–185.
36 M. L. Di Lorenzo, R. Ovyn, M. Malinconico, P. Rubino and Y. Grohens, *Polym. Eng. Sci.*, 2015, **55**, 2698–2705.
37 C. Zeng, N.-W. Zhang, S.-Q. Feng and J. Ren, *J. Therm. Anal. Calorim.*, 2013, **111**, 633–646.
38 M. Dobrzyńska-Mizera, M. Knitter, D. Szymanowska, S. Mallardo, G. Santagata and M. L. Di Lorenzo, *J. Appl. Polym. Sci.*, 2022, **139**, 52177.
39 S. Minardi, B. Corradetti, F. Taraballi, M. Sandri, J. Van Eps, F. J. Cabrera, B. K. Weiner, A. Tampieri and E. Tasciotti, *Biomaterials*, 2015, **62**, 128–137.
40 N. Shanmugasundaram, P. Ravichandran, P. Neelakanta Reddy, N. Ramamurty, S. Pal and K. Panduranga Rao, *Biomaterials*, 2001, **22**, 1943–1951.
41 A. R. Berens and I. M. Hodge, *Macromolecules*, 1982, **15**, 756–761.
42 V. M. Boucher, D. Cangialosi, A. Alegría and J. Colmenero, *Phys. Chem. Chem. Phys.*, 2017, **19**, 961–965.
43 R. Androsch, C. Schick and M. L. Di Lorenzo, *Macromol. Chem. Phys.*, 2014, **215**, 1134–1139.
44 M. C. Righetti, M. Gazzano, M. L. Di Lorenzo and R. Androsch, *Eur. Polym. J.*, 2015, **70**, 215–220.
45 M. L. Di Lorenzo, P. Rubino, R. Luijkx and M. Hélou, *Colloid Polym. Sci.*, 2014, **292**, 399–409.
46 M. L. Di Lorenzo, P. Rubino, B. Immirzi, R. Luijkx, M. Hélou and R. Androsch, *Colloid Polym. Sci.*, 2015, **293**, 2459–2467.
47 P. Comodi, Y. Liu, P. F. Zanazzi and M. Montagnoli, *Phys. Chem. Miner.*, 2001, **28**, 219–224.
48 M. Cocca, M. L. D. Lorenzo, M. Malinconico and V. Frezza, *Eur. Polym. J.*, 2011, **47**, 1073–1080.
49 K. A. Thomas, J. M. Toth, N. R. Crawford, H. B. Seim, L. L. Shi, M. B. Harris and A. S. Turner, *Spine*, 2008, **33**, 734–742.
50 J. Y. Lazennec, A. Madi, M. A. Rousseau, B. Roger and G. Saillant, *Eur. Spine J.*, 2006, **15**, 1545–1553.
51 A. Smieszek, K. Marycz, K. Szustakiewicz, B. Kryszak, S. Targonska, K. Zawisza, A. Watras and R. J. Wiglusz, *Mater. Sci. Eng., C*, 2019, **98**, 213–226.
52 R.-G. Guan, I. Johnson, T. Cui, T. Zhao, Z.-Y. Zhao, X. Li and H. Liu, *J. Biomed. Mater. Res., Part A*, 2012, **100**, 999–1015.
53 K. Joszko, M. Gzik, W. Wolański, B. Gzik-Zroska and E. Kawlewska, *J. Appl. Biomed.*, 2018, **16**, 51–58.
54 K. Dowgierd, R. Pokrowiecki, W. Wolanski, E. Kawlewska, M. Kozakiewicz, J. Wos, M. Dowgierd and Ł. Krakowczyk, *Oral Oncol.*, 2022, **127**, 105800.
55 K. Ficek, J. Rajca, M. Stolarz, E. Stodolak-Zych, J. Wieczorek, M. Muzalewska, M. Wyleżoł, Z. Wróbel, M. Binkowski and S. Błażewicz, *Polymers*, 2019, **11**, 1961.
56 J. Rajca, M. Gzik and K. Ficek, *Appl. Sci.*, 2021, **11**, 2482.
57 E. Pietka and A. Gertych, *Comput. Med. Imaging. Graph.*, 2021, **89**, 101891.
58 M. Muzalewska, *Appl. Sci.*, 2021, **11**, 11070.
59 *Handbook of Research on Interactive Information Quality in Expanding Social Network Communications*, F. V. Cipolla-Ficarra, ed., IGI Global, 2015.
60 PN-EN_ISO_2039-1:2004.
61 PN-EN_ISO 1183-1:2019-05.

